hydrogen

MDPI

Article

Bifunctional NiCo/rGO Bimetallic Nanocomposites for Efficient Alkaline Hydrogen and Oxygen Evolution Reaction

Kumaresan Natesan [1,*], Alberto Bacilio Quispe Cohaila [1,*], Elisban Juani Sacari Sacari [2] and Mangalaraja Ramalinga Viswanathan [3]

[1] GIMAECC Research Group, Faculty of Engineering, Jorge Basadre Grohmann National University, Av. Miraflores S/N, Tacna 23003, Peru
[2] Faculty of Sciences, National University of Engineering, Av. Túpac Amaru 210, Lima 15333, Peru
[3] Faculty of Engineering and Architecture, Universidad Arturo Prat, Avenida Arturo Prat 2120, Iquique 1110939, Chile; mramalinga@unap.cl
* Correspondence: kumaresanphy@gmail.com (K.N.); aquispec@unjbg.edu.pe (A.B.Q.C.)

Abstract

Recently, efficient and robust electrocatalysts for alkaline HER and OER are essential for water splitting applications. In the present work, the combination of nickel (Ni) and cobalt (Co) bimetallic nanocomposites embedded on rGO were prepared by the solid-state sintering process. X-ray diffraction analysis shows a single face–centered–cubic metallic phase together with the (002) diffraction of reduced graphene oxide (rGO), consistent with the NiCo phase being supported on rGO. The field emission scanning electron microscopy analysis shows sub-micrometer metallic particles anchored on the layered rGO sheets in the NiCo/rGO bimetallic nanocomposite. The core-level spectrum of Ni and Co metals confirmed the existence of more oxidation on the surface of rGO. The NiCo/rGO bimetallic nanocomposites show an OER overpotential at 10 mA/cm^2 of 358 mV vs. RHE and a Tafel slope of 92 mV/dec. The HER overpotential is observed at 10 mA/cm^2 of −136 mV vs. RHE with a Tafel slope of 95 mV/dec. Both HER and OER stability analyses were performed for 25 h. Finally, full cell analysis of NiCo/rGO revealed that it requires 1.9 V to reach 10 mA/cm^2 and shows stable operation for 10 h. The present work paves the way for the formation of NiCo/rGO bimetallic nanocomposites for bifunctional electrocatalytic applications.

Keywords: metals; reduced graphene oxide; bimetallic nanocomposites; hydrogen evolution reaction; oxygen evolution reaction

Check for updates

Academic Editor: Yuxuan Xiao

Received: 14 August 2026
Revised: 16 September 2026
Accepted: 17 September 2026
Published: 19 September 2026

Copyright: © 2026 by the authors. Licensee MDPI, Basel, Switzerland. This article is an open access article distributed under the terms and conditions of the Creative Commons Attribution (CC BY) license.

1. Introduction

In the last two decades, the population and development of industrialization have increased the global energy demand, which will increase continuously in the foreseeable future in the twenty-first century [1]. At present, nonrenewable energy sources of fossil fuels, coal, oil, and natural gas have fulfilled a significant portion of the world energy demand. Meanwhile, limitless usage of fossil fuels is gradually diminishing, and the environmental concerns arising from their widespread use have prompted significant research toward the development of advanced technologies to harvest clean and sustainable energies from renewable sources, including solar and wind energy [2,3]. Thus, researchers are focused on alternative ways, such as eco-friendly and renewable energy source processes, to replace and reduce the utilization of fossil fuels [4]. Although abundant solar energy and wind

energy are sustainable energy sources and can be converted into electricity, they are intermittent and dependent on weather conditions. To mitigate the challenges posed by the intermittent availability of renewable energy, the electrocatalytic generation of hydrogen (H_2) through water splitting has been widely recognized as an attractive pathway for clean energy conversion and storage [5–7]. Hydrogen has been considered as a potential energy source due to its high gravimetric energy density, eco friendliness, and zero carbon dioxide emissions [8–10]. Electrocatalytic water splitting is a promising strategy, which consists of the half reactions at the cathode and anode for the hydrogen evolution reaction (HER) and the oxygen evolution reaction (OER), respectively [11–13]. However, HER and OER follow two-electron and four-electron-proton energy transfer pathways, respectively, which cause large kinetic energy barriers; thereby, overall water splitting kinetics are substantially slow [14].

However, the slow kinetics and large overpotentials effectively suppress the overall water splitting (OWS) process because it is a thermodynamically uphill reaction. Therefore, the design and synthesis of remarkable electrocatalysts with excellent electrocatalytic performance exhibiting a low overpotential is an immediate need for OWS application. An ideal electrocatalyst for OWS should satisfy two essential requirements: high catalytic activity for both HER and OER, enabling the generation of large current densities at low overpotentials, and excellent long-term operational stability. Currently, platinum (Pt) is considered the benchmark electrocatalyst for HER, whereas noble metal oxides such as iridium dioxide (IrO_2) and ruthenium dioxide (RuO_2) are regarded as the most effective catalysts for OER [15,16]. However, their widespread commercial deployment is hindered by their scarcity, high cost, and insufficient long-term durability under practical operating conditions. Therefore, the development of cost-effective, highly efficient, and durable bifunctional electrocatalysts for OWS has become a critical research priority. Significant efforts have been devoted to designing non-precious metal-based electrocatalysts with enhanced HER and OER activities [5]. Such catalysts can mitigate the adverse crossover effects associated with using different electrode materials, simplify electrolyze design, and reduce the overall cost of device fabrication [17]. Consequently, significant research efforts have been directed toward the development of advanced bifunctional electrocatalysts for OWS. To achieve this goal, a wide range of transition metal-based electrocatalysts, including transition metal nitrides (TMNs) [18], transition metal carbides (TMCs) [19], transition metal phosphides (TMPs) [20], transition metal sulfides (TMSs) [21], transition metal borides (TMBs) [22], transition metal hydroxides (TMHs) [23], and transition metal oxides (TMOs) [24], have been extensively investigated as promising candidates for OWS. Among them, bimetallic nanoparticles embedded on carbon nanocomposites have attracted attention because their geometric and electronic structures can precisely be controlled due to their composition and phase structure [25].

In recent years, various bimetallic systems based on nickel (Ni) and cobalt (Co) materials have received significant attention due to their outstanding electrocatalytic properties and earth-abundant nature and undergo surface reconstruction during electrochemical operation in alkaline electrolyte, leading to the in situ formation of highly active NiCo layered (oxy)hydroxide species. These surface-generated phases exhibit excellent OER activity and, in some cases, can outperform commercial noble-metal-based OER catalysts. Moreover, NiCo-based materials have also shown considerable promise as HER electrocatalysts, making them attractive candidates for the development of efficient bifunctional catalysts for overall water splitting [26,27]. Further, NiCo bimetallic nanocomposites integrated with conductive carbon sheets will provide an effective pathway for both HER and OER electrocatalytic performance. The synergistic interaction between Ni and Co promotes the adsorption and desorption of reaction intermediates, increases the electrical conductivity,

provides a large specific surface area, and enhances mechanical stability, thereby optimizing the reaction kinetics and significantly improving catalytic activity [28,29]. Many synthesis methods were followed to prepare the NiCo/reduced graphene oxide (rGO) bimetallic nanocomposites and show better electrochemical performance. In this way, Saadet Dinç et al. [30] prepared NiCo/ERGO by electrochemical co-deposition on an ITO substrate. For HER, the overpotentials and Tafel slope were 47 mV and 80 mV; in acetic and alkaline medium, these values were 31 mV/dec and 202 mV/dec. The OER overpotential and Tafel slope were 275 mV and 73 mV/dec, and 1.54 V cell voltage was maintained for 24 h. Chen Yu et al. [31] prepared CoNi oxyhydroxide nanosheets [CoNi-OOH-30 (40)] by the electrodeposition method, showing overpotentials of −210 mV and 279 mV at 10 mA/cm^2, and Tafel slopes of 67 and 62 mV/dec for HER and OER in alkaline media. Further, the full cell analysis of CoNi-OOH-30(40) requires 1.76 V for 10 mA/cm^2.

Based on this inspiration, the simple solid-state sintering process is an easy, effective, and environmentally friendly method, and there are no considerable reports on this method. Hence, in the present work, Ni, Co, NiCo, and NiCo/rGO bimetallic nanocomposites were prepared by the solid-state sintering process under a nitrogen atmosphere. The XRD analysis confirms NiCo bimetallic nanocomposites were embedded on the rGO. The FESEM analysis shows the combined structure of NiCo bimetallic nanocomposite formation on rGO sheets. The NiCo/rGO bimetallic nanocomposites show an OER overpotential at 10 mA/cm^2 of 358 mV vs. reversible hydrogen electrode (RHE) with a Tafel slope of 92 mV/dec and an HER overpotential at 10 mA/cm^2 of −136 mV vs. RHE with a Tafel slope of 95 mV/dec, with 25 h of continuous operation. Finally, full cell analysis of NiCo/rGO revealed that it requires 1.9 V to reach 10 mA/cm^2 and shows better performance for 10 h.

2. Materials, Methods, and Characterization

Detailed information of the materials (Purchased from Sigma-Aldrich, Burlington, MA, USA), the synthesis method of graphene oxide (GO) and rGO (Figure S1), and NiCo bimetallic nanocomposites embedded on rGO and their characterization techniques are given in the Supporting Information Section S1.

3. Results and Discussion

3.1. X-Ray Diffraction Analysis

The X-ray diffraction (XRD) analysis of GO and rGO is presented in Figure S2. The prepared metallic Ni is evaluated for XRD analysis, and the optimized results are presented in Figure 1. The XRD pattern of Ni shows peaks at 44.50°, 51.47°, 76.26°, 92.50°, and 98.10°, which correspond to the (111), (200), (220), (311), and (222) planes, respectively, and the XRD pattern matches well with Joint Committee on Powder Diffraction Standards (JCPDS) card 04-0850 (Figure 1a). The crystallite size of the Ni metal, calculated from the (111) plane, is 6.85 nm, and the interplanar value is observed at 0.203 nm. The XRD pattern of metallic Co shows diffraction peaks at 41.32°, 44.14°, 47.09°, 62.47°, 75.69°, and 83.66° that correspond to the (100), (002), (101), (102), (110), and (103) planes, and the XRD pattern matches well with the hexagonal close-packed (hcp) of Co metallic nature with the JCPDS card No. 05-0727 (Figure 1b). Further, the crystallite size and interplanar distance of the Co metal are 5.50 nm and 0.205 nm, respectively.

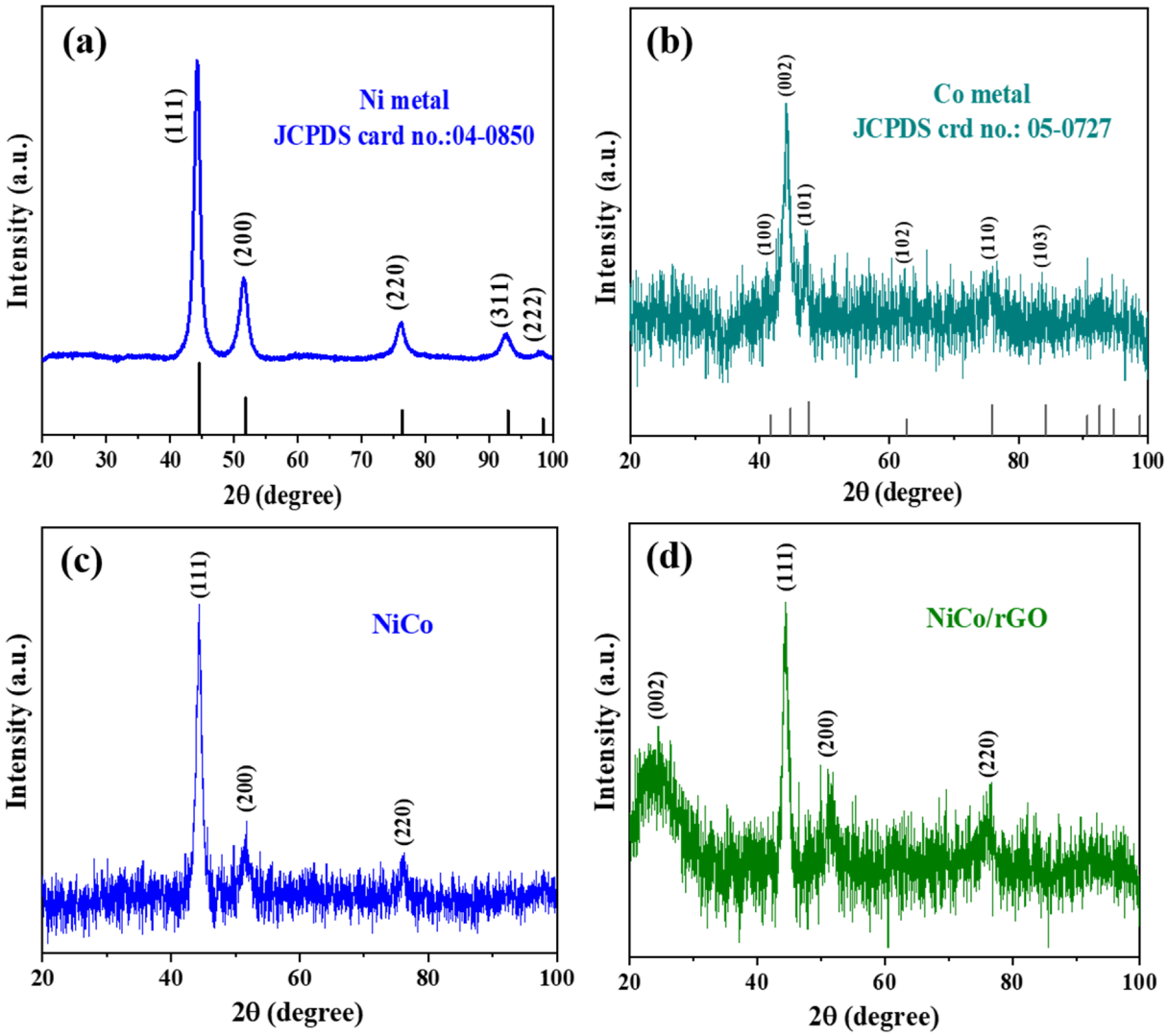


Figure 1. XRD pattern of (**a**) Ni; (**b**) Co; (**c**) NiCo; and (**d**) NiCo/rGO bimetallic nanocomposites.

Figure 1c shows that the XRD peaks at 44.34°, 51.69°, and 76.07° are related to the (111), (200), and (220) planes, respectively, which confirms the formation of NiCo bimetallic nanocomposites. Further, crystallite size and interplanar distance are calculated for NiCo bimetallic nanocomposites at 44.34° and are 6.82 nm and 0.204 nm, respectively. The XRD analysis of NiCo/rGO is presented in Figure 1d, which shows that the diffraction peaks at 44.54°, 51.65°, and 75.65° are related to the (111), (200), and (220) planes of NiCo bimetallic nanocomposites, respectively. Additionally, the crystallite size and interplanar distance calculated from this nanocomposite peak are 8.01 nm and 0.203 nm, respectively. Furthermore, the broad peak observed at 24.10° is related to the (002) plane of rGO. Hence, the pattern indexes as a single face-centered-cubic metallic phase; this, together with the rGO reflection, is consistent with the formation of rGO-supported NiCo bimetallic nanocomposites. It should be noted that the precision in the lattice parameter attainable under the present measurement conditions does not permit the degree of Co substitution in the cubic lattice to be quantified by Vegard analysis, since the full range between fcc Ni (3.5240 Å) and fcc Co (3.5447 Å) is only 0.021 Å. The results are therefore consistent with the formation of a NiCo solid solution but do not exclude an intimate mixture of phases below the detection limit of the measurement. The XRD pattern of GO and rGO is discussed in Supporting Information Section S2.

3.2. Field Emission Scanning Electron Microscopic Analysis

The morphological analysis of GO and rGO was evaluated using field emission scanning electron microscopic (FESEM) analysis, and it is presented in Supporting Information (Figure S3).

FESEM images of metallic Ni at different magnifications are presented in Figure 2. Figure 2a confirms the metallic Ni with a needle-like structure, which contains well-developed Ni particle assembly and branched needle structures. The synthesized Co metal nanoparticle exhibits a well-developed spherical structure with a size of 750 to 1000 nm (Figure 2b). The FESEM images of the NiCo bimetal are presented in Figure 2c, which confirm the formation of NiCo bimetallic nanocomposites with the combined structure of needle-like Ni with a spherical structure of Co. This confirms the well-developed NiCo bimetallic nanocomposite structure. The FESEM image of the NiCo/rGO composite is presented in Figure 2d, which confirms the presence of NiCo-bimetallic nanocomposites with rGO. From the FESEM analysis, NiCo bimetals are combined with the lamellar structure of the rGO to form NiCo/rGO bimetallic nanocomposites.

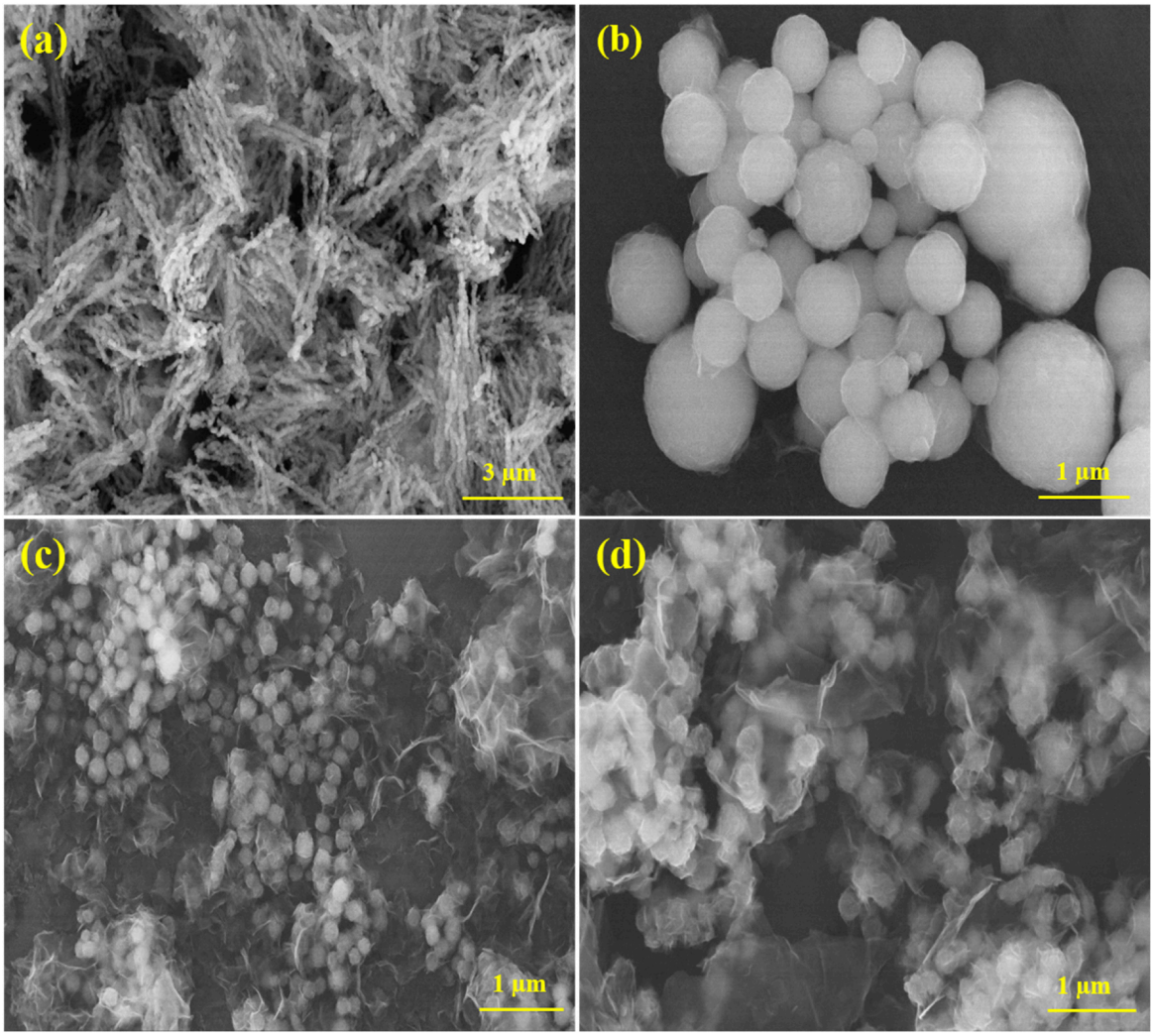


Figure 2. FESEM analysis: (**a**) Ni; (**b**) Co; (**c**) NiCo; and (**d**) NiCo/rGO bimetallic nanocomposites.

Further, the elemental mapping analysis was carried out for NiCo/rGO bimetallic nanocomposites, which shows the presence of Ni, Co, C, and O elements in the nanocomposites (Figure 3a–f). Additionally, energy dispersive X-ray analysis (EDXA) was carried out for NiCo/rGO bimetallic nanocomposites, which confirmed the presence of Co, Ni, O,

and C elements along with the weight % of 37.81%, 36.11%, 17.05%, and 9.03%, respectively (Figure 3g).

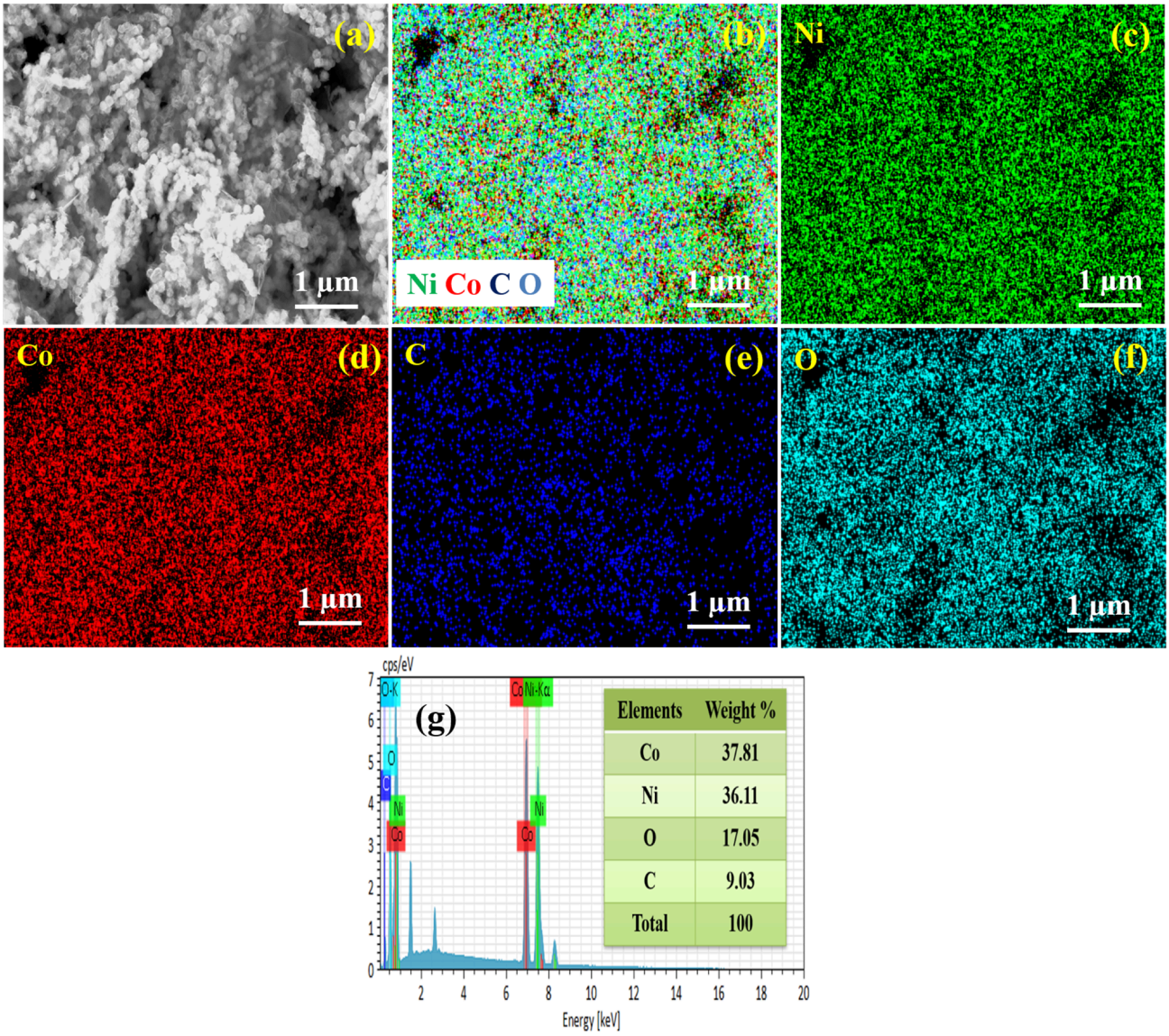


Figure 3. Elemental mapping analysis of NiCo/rGO: (**a**) corresponding FESEM image; (**b**) presence of elements in the combined formation; (**c**–**f**) Ni, Co, C, and O elements; and (**g**) EDXA analysis.

3.3. TEM Analysis

Transmission electron microscopy (TEM) images of GO and rGO are shown in Figure S4. The TEM analysis of NiCo/rGO bimetallic nanocomposites is presented in Figure 4a, which shows the combined structure of both needle-like Ni metals combined with the spherical shape of Co metals, which confirms the formation of NiCo bimetallic nanocomposites. Further, these NiCo bimetallic nanocomposites are embedded on the sheet-like structure of rGO, which confirms the strong interaction between the metals and rGO. Further, the high-resolution transition electron microscopic analysis (HRTEM) of the NiCo/rGO bimetallic nanocomposites is presented in Figure 4b, which reveals that the interlayer distances of 0.203 nm are related to the (111) plane of the NiCo bimetallic nanocomposites. HRTEM analysis confirmed the NiCo bimetallic nanocomposites combined with rGO.

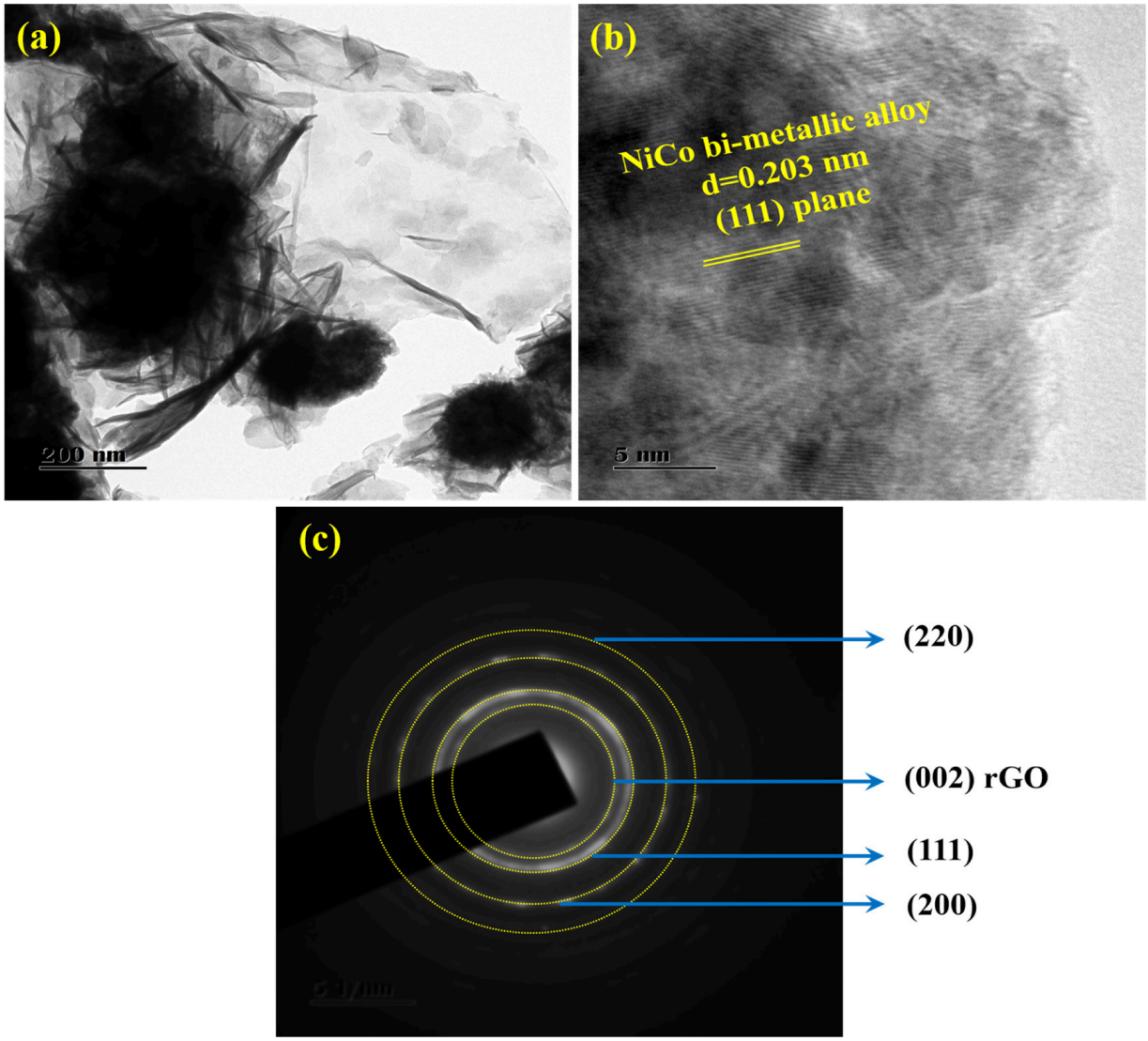


Figure 4. (**a**) TEM analysis of NiCo/rGO; (**b**) HRTEM analysis of NiCo/rGO; and (**c**) corresponding SAED pattern of NiCo/rGO.

Figure 4c shows the selected area electron diffraction (SAED) pattern of the NiCo/rGO bimetallic nanocomposites, which exhibits distinct concentric diffraction rings, confirming the polycrystalline nature. The diffraction rings were indexed with the crystalline nature of NiCo bimetallic nanocomposites and rGO. Further, the interplanar distances of 0.203 nm, 0.176 nm, and 0.125 nm are related to the (111), (200), and (220) planes of NiCo bimetallic nanocomposites. Additionally, the interplanar distance of 0.369 nm is related to the (002) plane of rGO. Coexistence of diffraction rings associated with both NiCo bimetallic nanocomposites and rGO demonstrates the successful incorporation of NiCo bimetallic nanocomposites onto the rGO sheets.

3.4. XPS Analysis

The X-ray photoelectron spectroscopy analysis (XPS) analysis of NiCo/rGO bimetallic nanocomposites was examined, and the obtained results are presented in Figure 5. The survey spectrum of NiCo/rGO bimetallic nanocomposites is presented in Figure 5a. The core-level spectrum of Ni shows two main districts at around ~852.07 eV and ~869.59 eV due to spin–orbit splitting of $Ni2p_{3/2}$ and $Ni2p_{1/2}$, respectively, and the difference in the binding energy is 17.52 eV. Further, Ni $2p_{3/2}$ shows three deconvoluted peaks at 854.21 eV,

856.31 eV, and 860.81 eV, corresponding to the Ni^{2+} and Ni^{3+} oxidation states and the satellite peak, respectively [32]. Similarly, Ni $2p_{1/2}$ shows three deconvoluted peaks at 871.71 eV, 873.41 eV, and 878.81 eV, corresponding to Ni^{2+} and Ni^{3+} oxidation states and the satellite peak, respectively [33] (Figure 5b). Figure 5c shows the core-level Co 2p spectrum, which contains two main regions at around ~777.59 eV and ~793.04 eV due to spin–orbit splitting of Co $2p_{3/2}$ and Co $2p_{1/2}$, respectively, separated by 15.45 eV. Co $2p_{3/2}$ shows three peaks at 779.41 eV, 781.31 eV, and 784.51 eV, corresponding to the Co^{3+} and Co^{2+} oxidation states and the satellite peak, respectively [33]. Co $2p_{1/2}$ shows three peaks at 795.21 eV, 797.81 eV, and 801.61 eV that correspond to Co^{3+} and Co^{2+} oxidation states and the satellite peak, respectively [33]. The C1s core-level spectrum is shown in Figure 5d, which reveals that the three peaks at 284.81 eV, 286.81 eV, and 289.61 eV are related to C-C, C-O and O-C=O, respectively [34]. The core-level spectrum of O1s is deconvoluted into three peaks (Figure 5e); the observed peak at 529.41 eV is attributed to the oxygen bond with the NiCo/rGO matrix or in the hydroxide formation. The peak observed at 531.07 eV is due to the formation of −OH vacancies. Finally, the peak located at 532.21 eV is due to adsorbed C-O/adsorbed H_2O on the NiCo/rGO matrix [35]. It is important to note in the present work that the core-level spectrum of Ni and Co metals confirms the existence of more oxidation states on the surface of rGO, which may be used to improve the electrochemical activity during the HER and OER analysis.

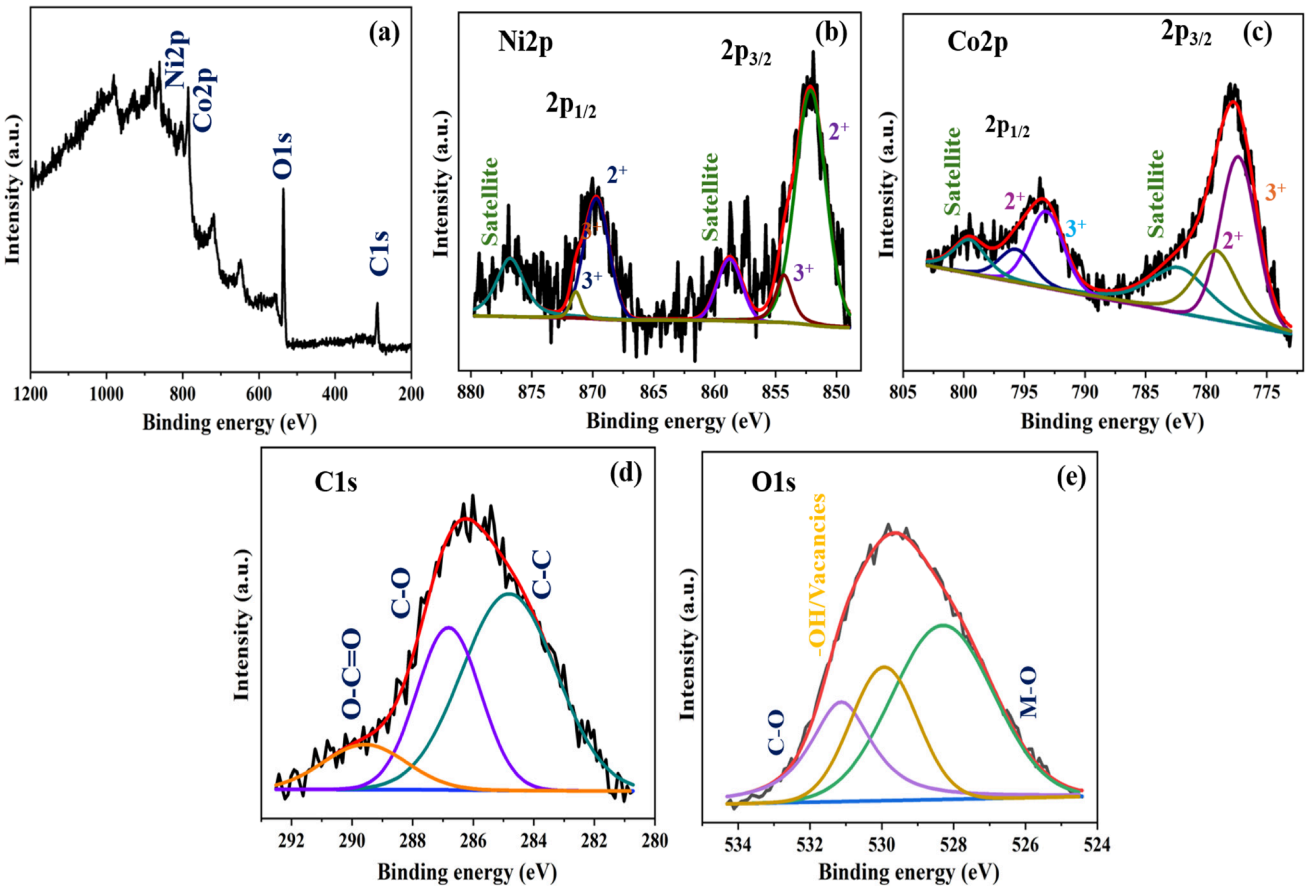


Figure 5. XPS analysis of NiCo/rGO bimetallic nanocomposites: (**a**) survey spectra; and (**b**–**e**) core-level spectra of Ni2p, Co2p, C1s, and O1s.

3.5. Electrochemical OER Analysis

The synthesized nanoparticles were used for the OER analysis by using 1 M potassium hydroxide (KOH) as an electrolyte solution, and the obtained results are presented in Figure 6. During the OER analysis, the synthesized Ni, Co, NiCo, and NiCo/rGO show

onset potentials of 1.624 V, 1.821 V, 1.609 V, and 1.505 V vs. RHE (Figure 6a). The benchmark material of RuO_2 shows the onset potential of 1.503 V vs. RHE. In the present work, the synthesized NiCo/rGO bimetallic nanocomposites requires a relatively low onset potential of 1.505 V vs. RHE. Further, Figure 6b shows the Tafel slope values of Ni, Co, NiCo, NiCo/rGO, and RuO_2 are 108 mV/dec, 119 mV/dec, 104 mV/dec, 92 mV/dec, and 86 mV/dec, respectively. The NiCo/rGO nanocomposite shows an enhancement of water reduction kinetics; thereby, the OER performance is increased in the alkaline medium. The comparative analysis is given in Figure 6c, which shows the onset potential (current 10 mA/cm^2) and overpotential (vs. RHE) for Ni, Co, NiCo NiCo/rGO, and RuO_2. The potentials of Ni, Co, NiCo, NiCo/rGO, and RuO_2 are observed at 10 mA/cm^2 current density, which reveals the potentials of 1.698 V, 1.900 V, 1.663 V, 1.588 V, and 1.570 V vs. RHE, respectively. The overpotentials at 10 mA/cm^2 for Ni, Co, NiCo, NiCo/rGO, and RuO_2 are 468 mV, 672 mV, 433 mV, 358 mV, and 340 mV, respectively. The overpotentials of NiCo/rGO bimetallic nanocomposites exhibit an enhancement of OER performance when compared with that of bare Ni and Co metals and NiCo bimetal. The stability of the NiCo/rGO bimetallic nanocomposites is evaluated through the chronoamperometric analysis for a period of 25 h (Figure 6d). During this analysis, the given input potential is 1.588 V, which provides a current density at around 10 mA/cm^2 for 25 h, which confirms better stability of NiCo/rGO bimetallic nanocomposites in the alkaline medium. Electrochemical impedance spectroscopy (EIS) measurement is used to analyze the charge transport and interfacial electron–transfer interaction of Ni, Co, NiCo, and NiCo/rGO electrocatalysts toward the oxygen evolution reaction (OER). The fitted Nyquist plot is used to evaluate the solution resistance (R_s) and charge transfer resistance (R_{ct}). The charge transfer resistance (R_{ct}), obtained from the diameter of the semi-circle in the high-frequency region, was determined to be 8.2 Ω, 6.2 Ω, 6.0 Ω, and 4.8 Ω for Ni, Co, NiCo, and Ni-Co/rGO, respectively (Figure 6e). The gradual decrease in R_{ct} from Ni to NiCo/rGO indicates a significant improvement in the charge-transfer kinetics at the electrode/electrolyte interface. The NiCo/rGO electrode exhibits the lowest R_{ct} value of 4.8 Ω, demonstrating the fastest electron-transfer process and the most favorable reaction kinetics for OER. This enhanced electrochemical behavior can be attributed to the synergistic effect between the bimetallic NiCo active centers and the highly conductive rGO framework, which facilitates rapid electron transport and improves the accessibility of catalytic active sites. Furthermore, the lower impedance response of the NiCo/rGO electrode suggests reduced energy barriers for charge transfer and enhanced electrical conductivity, thereby accelerating the OER process. In contrast, the higher R_{ct} value observed for the pristine Ni electrode reflects slower interfacial electron-transfer kinetics. Therefore, the EIS results clearly demonstrate that the incorporation of Co and rGO effectively improves the electrical conductivity and charge–transfer characteristics of the catalyst, which is consistent with the superior OER activity exhibited by the NiCo/rGO bimetallic nanocomposites. Further, the electrochemical double layer capacitance (C_{dl}) is carried out for Ni, Co, NiCo, and NiCo/rGO bimetallic nanocomposites, and the obtained results are presented in Figure S5.

In the OER process, the synthesized NiCo/rGO bimetallic nanocomposites show a Tafel slope value of 92 mV/dec, which confirms favorable OER reaction kinetics. Initially, during anodic polarization, Ni and Co species in NiCo/rGO undergo electrochemical surface oxidation and reconstruction.

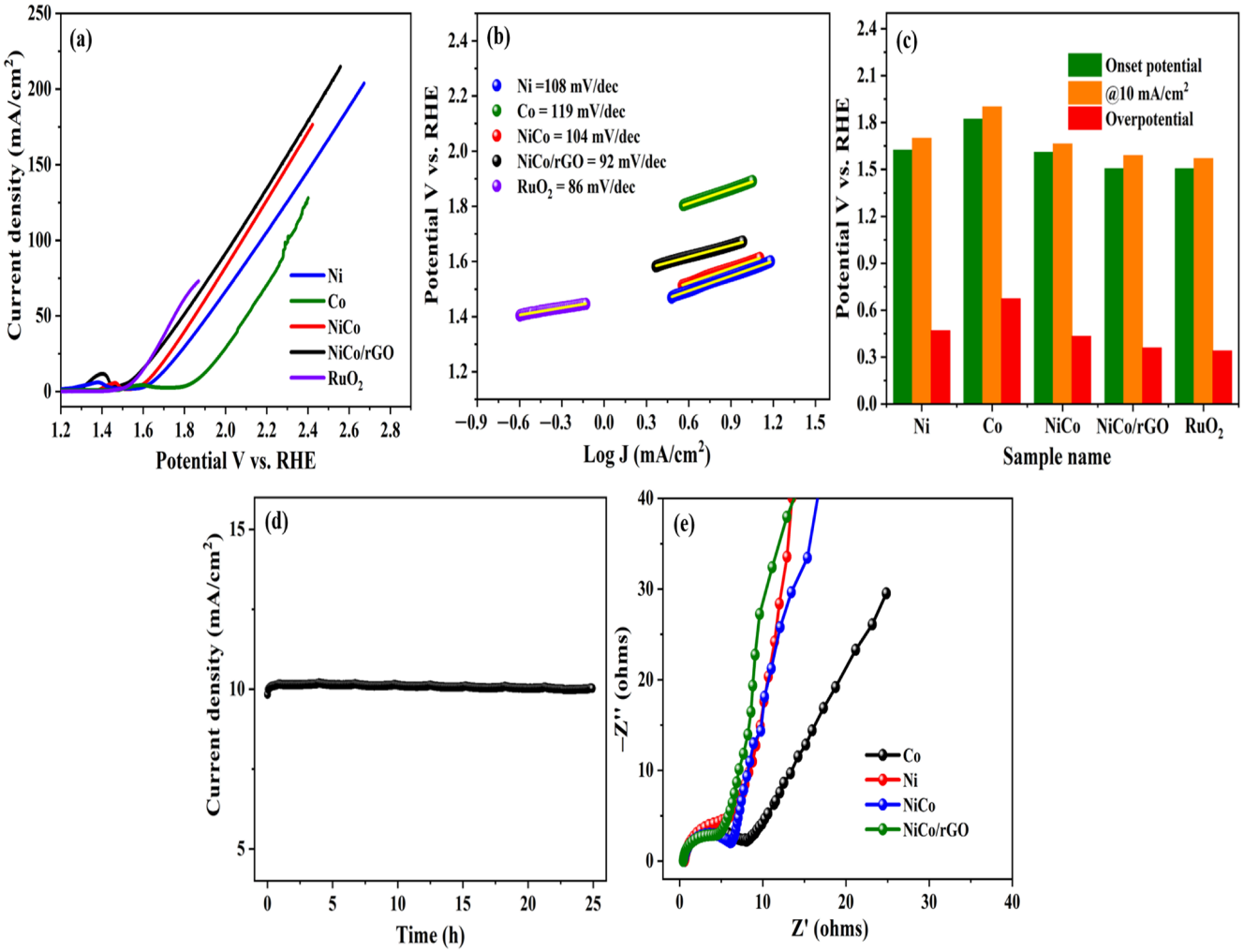


Figure 6. OER analysis of Ni, Co, NiCo, and NiCo/rGO: (**a**) LSV polarization curve; (**b**) Tafel plot; (**c**) Bar chart comparison of the onset potential, the potential required to reach 10 mA/cm^2 current density, and the overpotential; (**d**) Chronoamperometry analysis of NiCo/rGO for 25 h; and (**e**) EIS analysis.

Notably, the XPS analysis also confirmed that the Ni and Co metals show the different oxidation states of Ni^{2+}, Ni^{3+} and Co^{3+}, Co^{2+}. Further, during the OER analysis, Ni and Co metals generate NiOOH- and CoOOH-like active species, and these surface-active species are favorable for the sequential adsorption and conversion of OH^- into oxygenated intermediates, including OH^*, O^*, and OOH^*, followed by O_2 evolution [36].

$$OH^- + * \rightarrow OH^* + e^- \quad (1)$$

$$OH^* + OH^- \rightarrow O^* + H_2O + e^- \quad (2)$$

$$O^* + OH^- \rightarrow OOH^* + e^- \quad (3)$$

$$OOH^* + OH^- \rightarrow O_2 + H_2O + e^- \quad (4)$$

Additionally, rGO enhances electron conductivity, reduces agglomeration, and improves the effective dispersion of the NiCo active phase. Therefore, synergistic Ni-Co work as catalytic centers and rGO improves the efficient charge transfer process and accelerates OER kinetics.

3.6. Electrochemical HER Analysis

HER analysis was carried out for Ni, Co, NiCo, and NiCo/rGO, and the obtained results are presented in Figure 7. The linear sweep voltammetry (LSV) analysis of Ni, Co, NiCo, NiCo/rGO, and benchmark Pt/C is presented in Figure 7a. The LSV analysis shows the onset potential at −0.134 V, −0.317 V, −0.098 V, −0.059 V, and −0.005 V vs. RHE, respectively, for Ni, Co, NiCo, NiCo/rGO, and Pt/C (Figure 7a). Figure 7b shows the Tafel slope values for Ni, Co, NiCo, and NiCo/rGO and Pt/C, respectively, which are 109 mV/dec, 115 mV/dec, 103 mV/dec, 95 mV/dec, and 83 mV/dec, respectively. NiCo/rGO shows enhancement of water reduction kinetics; thereby, the HER performance is increased in the alkaline medium. Figure 7c shows the comparative analysis of the onset potential (current at 10 mA/cm$^{2)}$ and the overpotential. The overpotentials at 10 mA/cm^2 for Ni, Co, NiCo, NiCo/rGO, and Pt/C are 256 mV, 407 mV, 160 mV, 136 mV, and 23 mV vs. RHE, respectively. Notably, the onset potential and overpotential of NiCo/rGO bimetallic nanocomposites exhibit an enhancement of HER performance when compared with that of bare Ni and Co metals. Further, NiCo/rGO has better HER performance; hence, the chronoamperometry analysis is carried out to analyze the electrode stability, and an applied potential of −0.136 V vs. RHE was held for 25 h (Figure 7d). The current density rises during the first hours, which is attributed to electrode activation through wetting of the carbon cloth and removal of the residual binder from the surface, and subsequently remains stable for the rest of the test. Hence, the synthesized NiCo/rGO bimetallic nanocomposites show better stability during HER analysis in the alkaline medium. The R_{ct} values of the synthesized samples are obtained from the EIS analysis through the Nyquist plot. The synthesized Ni, Co, NiCo, and NiCo/rGO reveal the corresponding R_{ct} values are 7.79 Ω, 6.42 Ω, 6.04 Ω, and 4.66 Ω, respectively (Figure 7e).

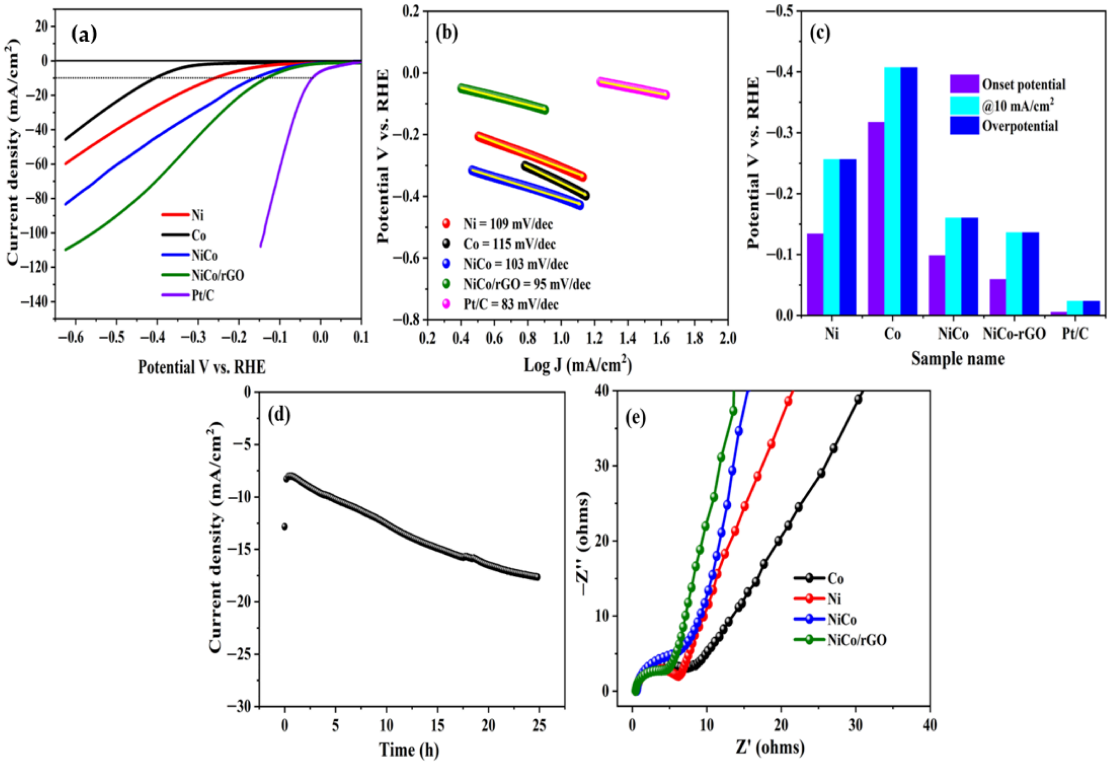


Figure 7. HER analysis of Ni, Co, NiCo, and NiCo/rGO: (**a**) LSV polarization curve; (**b**) Tafel plot; (**c**) Bar chart comparison of the onset potential, the potential required to reach 10 mA/cm^2 current density, and the overpotential; (**d**) Chronoamperometry analysis of NiCo/rGO for 25 h; and (**e**) EIS analysis.

Notably, the NiCo/rGO nanocomposite exhibits a relatively low R_{ct} value of 4.66 Ω, which confirms more efficient interfacial electron transfer and faster charge-transfer kinetics at the electrode/electrolyte interface. The improved charge-transfer property enhanced synergistic interaction between Ni and Co along with rGO, which improved the electron transport property and then enhanced HER performance.

Further, the electrochemical double layer capacitance (C_{dl}) is measured, and results are presented in Figure S6a–d. The Ni-Co/rGO catalyst exhibits significantly enhanced activity compared to the other monometallic counterparts, demonstrating the beneficial synergistic interaction between Ni and Co active sites. The NiCo/rGO bimetallic nanocomposite analysis requires a relatively low overpotential to achieve a current density of 10 mA/cm^2, indicating improved catalytic efficiency toward OER and HER performance. Further, the corresponding Tafel slope is markedly reduced, suggesting accelerated reaction kinetics and favorable charge transfer processes between electrode–electrolyte interface. This improved electrochemical performance confirms the strong electronic coupling interaction between Ni-Co bimetallic nanoparticles. Additionally, the conductive layer of rGO effectively improves rapid electron transport and efficient proton reduction. A high surface area platform for the uniform dispersion of NiCo nanoparticles thereby exposes abundant active catalytic sites, and it is favorable for better electrochemical OER and HER analysis. The electrocatalytic water splitting analysis of NiCo/rGO bimetallic nanocomposites in alkaline medium was investigated based on the Tafel values. In the present work, the HER analysis and Tafel slope value of 95 mV/dec are closer to the Volmer regime, suggesting that water dissociation is an important kinetic limitation. In this process, HER proceeds through the Volmer step [37].

$$H_2O + e^- + * \rightarrow H^* + OH^- \quad (5)$$

Further, water molecules adsorb onto the Ni-Co active sites and undergo electrochemical dissociation to generate adsorbed H^* and OH^- intermediates. Further, the formation of H^* species is combined with H_2O through the Heyrovsky step or with another H^* through the Tafel step to generate H_2.

$$H^* + H_2O + e^- \rightarrow H_2 + OH^- \quad (6)$$

$$2H^* \rightarrow H_2 \quad (7)$$

Synergistic interaction between Ni and Co facilitates H_2O activation, while the conductive rGO framework encourages the rapid electron transport to the catalytic centers, thereby improving OER performance.

3.7. Full Cell Water Splitting Analysis

The synthesized NiCo/rGO bimetallic nanocomposites were analyzed for OER and HER performance, which shows better activity under the alkaline medium; hence, the NiCo/rGO bimetallic nanocomposite is used for the full cell analysis through the conventional two-electrode liquid cell. In this way, anodic and cathodic electrodes were fabricated (1×1 cm^2) with ~1.5 mg catalyst loading on carbon cloth, and 1 M of KOH was used as an electrolyte solution. Further, both the anode and cathode are immersed at 1 cm distance. The full cell analysis shows the potential of 1.9 V to reach the 10 mA/cm^2 current density (Figure 8a). Further, the chronoamperometry analysis is carried out with the input voltage of 1.9 V to evaluate the stability of the catalyst for the time duration of 10 h in 1 M of KOH electrolyte solution. The chronoamperometry analysis was performed at a constant current density of 10 mA/cm^2, which confirms the better stability of NiCo/rGO bimetallic nanocomposites during the electrochemical analysis (Figure 8b).

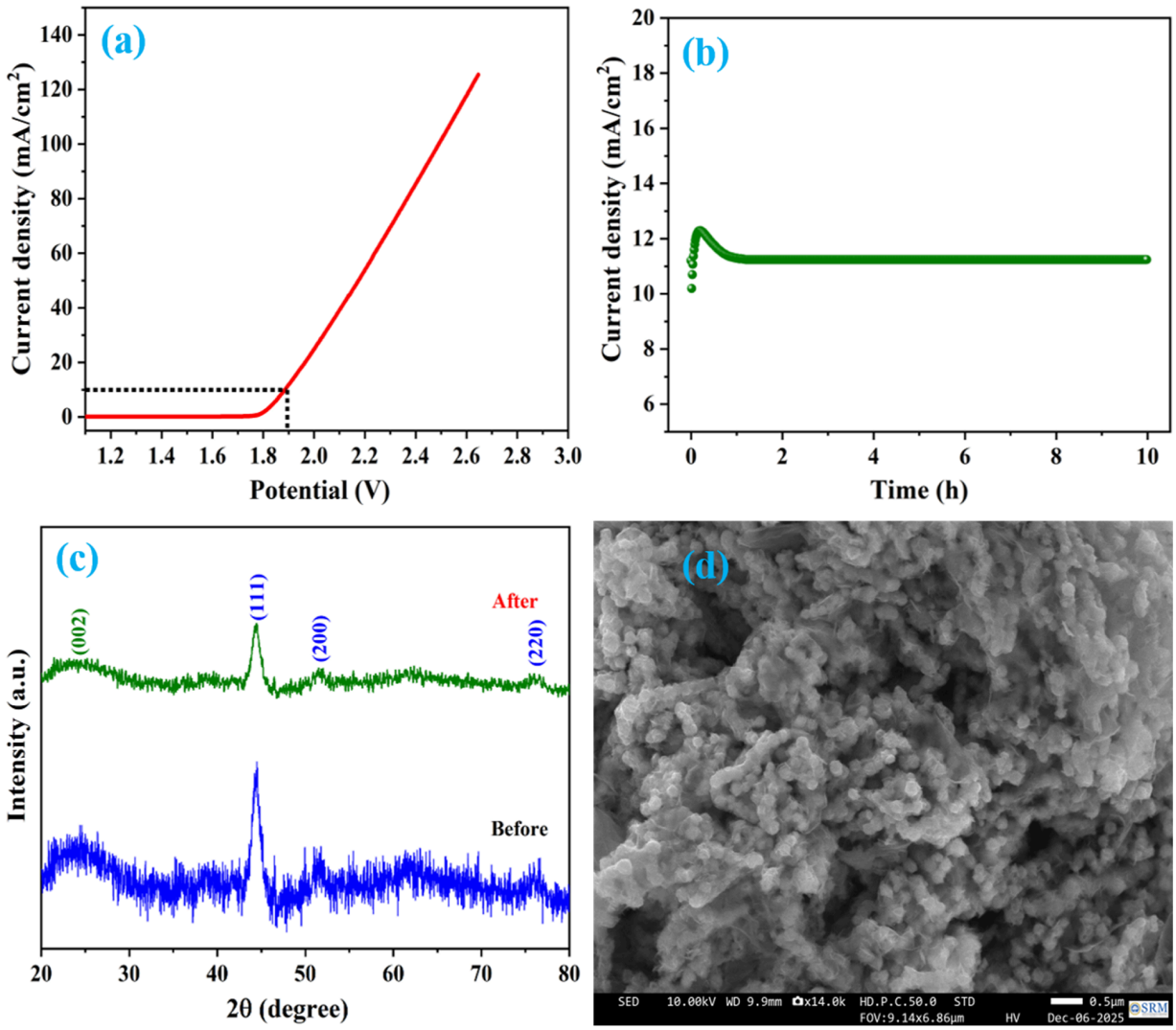


Figure 8. Full cell analysis of NiCo/rGO: (**a**) LSV analysis; (**b**) Chronoamperometry analysis for 10 h; and (**c**,**d**) Comparison of XRD and FESEM analysis of before and after full cell analysis.

Additionally, to confirm the structural and morphological properties, XRD and FE-SEM analysis were performed after the chronoamperometry analysis. The XRD analysis of NiCo/rGO shows the same crystallite pattern. There is no considerable change in the 2–theta angle; however, the intensity of the XRD is slightly reduced, which may be due to the influence of KOH during the electrochemical process (Figure 8c). Notably, FESEM analysis of NiCo/rGO shows stable morphology, which confirms that the before and after electrochemical analysis of NiCo/rGO is not affected by the influence of KOH (Figure 8d). Hence, the synthesized NiCo/rGO bimetallic nanocomposites show better performance during the electrochemical analysis, and they show better stability in the full cell analysis in the alkaline medium; thereby, the synthesized NiCo/rGO is recommended for electrochemical water splitting applications. The present results are compared with the previous reports and are presented in Table 1. Further, it is confirmed that the synthesis method is highly influenced by the crystallite phase, morphology, size, and electrical property of NiCo/rGO bimetallic nanocomposites; thereby, electrochemical analysis is effectively improved. The NiCo/rGO bimetallic nanocomposites were prepared by electrochemical deposition, and vapor deposition provides better performance, but the synthesis process is complicated. Hence, in the present work, we chose a simple step of the solid-state sintering process

under the nitrogen atmosphere. The synthesized NiCo/rGO bimetallic nanocomposites show better performance in 1 M KOH alkaline medium.

Table 1. Electrochemical comparative analysis of NiCo/rGO bimetallic nanocomposites.

Material	Method	HER (Overpotential/Tafel)	OER (Overpotential/Tafel)	Stability (h)	Full Cell Voltage	Author
NiCo/rGO	Electrochemical deposition	0.5 M H_2SO_4: 47 mV/31 mV/dec 1 M KOH: 80 mV/202 mV/dec	1 M KOH: 275 mV/73mV/dec	24 h (Full cell)	1.54 V	Saadet Dinc [30]
CoNi oxyhydroxide	Electrodeposition	1 M KOH: 210 mV/67 mV/dec	1 M KOH: 279 mV/62 mV/dec	60 h (Full cell)	1.76 V	Chen Yu [31]
MOF: CoNiP-CoNi-alloy	Carbonization and Phosphidation step	1 M KOH: 150 mV/97 mV/dec	1 M KOH: 300 mV/72 mV/dec	10 h (Full cell)	1.76 V	Paulraj Arunkumar [38]
NiCo/rGO	Electroless deposition	1 M KOH: 115 mV/45 mV/dec	-	10 h (HER)	-	Jing Dong [39]
MOF: NiCo	Vapor deposition	1 M KOH: 203 mV/152 mV/dec	1 M KOH: 168 mV/92 mV/dec	Multicurrent steps curve followed	1.42 V	Wenhua Zhang [40]
NiCo/rGO	Solid state sintering process	1 M KOH: 136 mV/95 mV/dec	1 M KOH: 358 mV/92 mV/dec	25 h (HER and OER); 10 h (full cell)	1.9 V	Present work

4. Conclusions

In brief, we synthesized Ni, Co, NiCo, and NiCo/rGO bimetallic nanocomposites by a simple sintering process in a tubular furnace under a nitrogen atmosphere. The XRD analysis of Ni and Co shows good metallic nature, the NiCo composite shows well-developed NiCo bimetallic nanocomposite formation. Further, XRD analysis of NiCo/rGO shows the presence of NiCo bimetallic nanocomposite formation along with the rGO crystallite, which confirms that the NiCo was embedded on rGO layers. The FESEM analysis of the monometallic Ni and Co samples shows needle-like and spherical structures, respectively, and rGO shows a layered morphology. In the NiCo/rGO composite, the metallic particles are anchored on the rGO sheets; the distinct structures of the two monometallic samples are not resolved separately within the composite. Additionally, TEM analysis confirms that the metallic particles are supported on the layered rGO structure in the NiCo/rGO bimetallic nanocomposite. The XPS analysis reveals the presence of Ni, Co, C, and O elements; Ni and Co show different oxidation states, 2^+ and 3^+, within the rGO structure. Importantly, the different oxidation states favorably improved the electrochemical activity. Further, this impact on NiCo/rGO bimetallic nanocomposites reduced their charge transfer resistance (Rct) and improved the electrochemical activity. During the OER analysis, synthesized NiCo/rGO showed an onset potential of 10 mA/cm^2 and overpotentials of 1.505 V, 1.588 V, and 358 mV vs. RHE, respectively. Further, the Tafel slope values of NiCo/rGO were 92 mV/dec. In the HER analysis, NiCo/rGO shows that the onset potential, overpotential, and Tafel slope were −59 mV, −136 mV vs. RHE, and 95 mV/dec, respectively. The full cell analysis of NiCo/rGO reveals better performance in alkaline medium, which requires 1.9 V to achieve 10 mA/cm^2 and shows better performance for 10 h. Additional XRD analysis reveals better structural and morphological stability. Based on the results obtained, the NiCo bimetallic nanocomposites embedded on rGO significantly improved the electrochemical performance; thereby, it confirms that the NiCo/rGO bimetallic nanocomposites are a useful material for bifunctional water splitting applications.

Supplementary Materials: The following supporting information can be downloaded at https://www.mdpi.com/article/10.3390/hydrogen7030136/s1, Figure S1: GO synthesis process using the improved method; Figure S2: X-ray diffraction analysis of GO and rGO; Figure S3: FESEM images of

GO and rGO; Figure S4: TEM images of GO and rGO; Figure S5: OER analysis, CV measurements of Ni, Co, NiCo, and NiCo/rGO, and the corresponding C_{dl} plot; Figure S6: HER analysis, CV measurements of Ni, Co, NiCo, and NiCo/rGO, and the corresponding C_{dl} plot. Refs. [40–43] are cited in SM.

Author Contributions: Conceptualization, methodology, writing—original draft preparation, K.N.; Supervision, funding acquisition, resources, A.B.Q.C.; Project administration, software, E.J.S.S.; Writing—review and editing, M.R.V.; All authors have read and agreed to the published version of the manuscript.

Funding: This work was funded by the National Council for Science, Technology and Technological Innovation (CONCYTEC) and the National Program for Scientific Research and Advanced Studies (PROCIENCIA) under the call "E067-2024-01 Special Projects: Incorporation of Postdoctoral Researchers in Peruvian Institutions" [Contract No. PE501092862-2024-PROCIENCIA] and research project "Perovskite–type $AtiO_3$ (A: Ca, Ni): Exploration of doping–induced defects for the improvement of hydrogen storage capacity" approved under Rectoral Resolution No. 13626-2024-UNJBG.

Data Availability Statement: The datasets produced and analyzed in this study are available from the corresponding author upon reasonable request.

Acknowledgments: N. Kumaresan acknowledges the National Council for Science, Technology and Technological Innovation (CONCYTEC) and the National Program for Scientific Research and Advanced Studies (PROCIENCIA) under the call "E067-2024-01 Special Projects: Incorporation of Postdoctoral Researchers in Peruvian Institutions" [Contract No. PE501092862-2024-PROCIEN-CIA]. Alberto Bacilio Quispe Cohaila acknowledges the National University Jorge Basadre Grohmann for funding the research project "Perovskite–type $ATiO_3$ (A: Ca, Ni): Exploration of doping–induced defects for the improvement of hydrogen storage capacity" approved under Rectoral Resolution No. 13626-2024-UNJBG. The author, Elisban Juani Sacari, gratefully acknowledges the financial support provided of CONCYTEC through the PROCIENCIA program under the "Scholarships for Doctoral Programs in Interinstitutional Alliances" competition, according to contracts N°PE501088673-2024-PROCIENCIA-BM and N°PE501084296-2023-PROCIENCIA-BM, for undertaking a doctoral program in physics at the National University of Engineering, Peru.

Conflicts of Interest: The authors declare no competing interests.

References

1. Scheffran, J.; Felkers, M.; Froese, R. Economic Growth and the Global Energy Demand. In *Green Energy to Sustainability*; John Wiley & Sons, Ltd.: Hoboken, NJ, USA, 2020; pp. 1–44, ISBN 978-1-119-15205-7.
2. Chu, S.; Majumdar, A. Opportunities and Challenges for a Sustainable Energy Future. *Nature* **2012**, *488*, 294–303. [CrossRef] [PubMed]
3. Yue, X.; Huang, S.; Cai, J.; Jin, Y.; Shen, P.K. Heteroatoms Dual Doped Porous Graphene Nanosheets as Efficient Bifunctional Metal-Free Electrocatalysts for Overall Water-Splitting. *J. Mater. Chem. A* **2017**, *5*, 7784–7790. [CrossRef]
4. Jiao, Y.; Zheng, Y.; Jaroniec, M.; Qiao, S.Z. Design of Electrocatalysts for Oxygen- and Hydrogen-Involving Energy Conversion Reactions. *Chem. Soc. Rev.* **2015**, *44*, 2060–2086. [CrossRef] [PubMed]
5. You, B.; Sun, Y. Chalcogenide and Phosphide Solid-State Electrocatalysts for Hydrogen Generation. *ChemPlusChem* **2016**, *81*, 1045–1055. [CrossRef] [PubMed]
6. Zhu, Y.P.; Guo, C.; Zheng, Y.; Qiao, S.-Z. Surface and Interface Engineering of Noble-Metal-Free Electrocatalysts for Efficient Energy Conversion Processes. *Acc. Chem. Res.* **2017**, *50*, 915–923. [CrossRef] [PubMed]
7. Chen, Z.; Ha, Y.; Jia, H.; Yan, X.; Chen, M.; Liu, M.; Wu, R. Oriented Transformation of Co-LDH into 2D/3D ZIF-67 to Achieve Co–N–C Hybrids for Efficient Overall Water Splitting. *Adv. Energy Mater.* **2019**, *9*, 1803918. [CrossRef]
8. Sun, H.; Yan, Z.; Liu, F.; Xu, W.; Cheng, F.; Chen, J. Self-Supported Transition-Metal-Based Electrocatalysts for Hydrogen and Oxygen Evolution. *Adv. Mater.* **2020**, *32*, 1806326. [CrossRef] [PubMed]
9. Ali, A.; Shen, P.K. Nonprecious Metal's Graphene-Supported Electrocatalysts for Hydrogen Evolution Reaction: Fundamentals to Applications. *Carbon Energy* **2020**, *2*, 99–121. [CrossRef]
10. Wang, J.; Zhong, H.; Wang, Z.; Meng, F.; Zhang, X. Integrated Three-Dimensional Carbon Paper/Carbon Tubes/Cobalt-Sulfide Sheets as an Efficient Electrode for Overall Water Splitting. *ACS Nano* **2016**, *10*, 2342–2348. [CrossRef] [PubMed]

11. Seh, Z.W.; Kibsgaard, J.; Dickens, C.F.; Chorkendorff, I.; Nørskov, J.K.; Jaramillo, T.F. Combining Theory and Experiment in Electrocatalysis: Insights into Materials Design. *Science* **2017**, *355*, eaad4998. [CrossRef] [PubMed]
12. Ali, A.; Shen, P.K. Recent Progress in Graphene-Based Nanostructured Electrocatalysts for Overall Water Splitting. *Electrochem. Energy Rev.* **2020**, *3*, 370–394. [CrossRef]
13. Zhang, J.; Zhang, Q.; Feng, X. Support and Interface Effects in Water-Splitting Electrocatalysts. *Adv. Mater.* **2019**, *31*, 1808167. [CrossRef] [PubMed]
14. Xiong, B.; Chen, L.; Shi, J. Anion-Containing Noble-Metal-Free Bifunctional Electrocatalysts for Overall Water Splitting. *ACS Catal.* **2018**, *8*, 3688–3707. [CrossRef]
15. Huang, L.; Wei, M.; Zaman, S.; Ali, A.; Xia, B.Y. Well-Connection of Micro-Platinum and Cobalt Oxide Flower Array with Optimized Water Dissociation and Hydrogen Recombination for Efficient Overall Water Splitting. *Chem. Eng. J.* **2020**, *398*, 125669. [CrossRef]
16. Yuan, Z.; Li, J.; Yang, M.; Fang, Z.; Jian, J.; Yu, D.; Chen, X.; Dai, L. Ultrathin Black Phosphorus-on-Nitrogen Doped Graphene for Efficient Overall Water Splitting: Dual Modulation Roles of Directional Interfacial Charge Transfer. *J. Am. Chem. Soc.* **2019**, *141*, 4972–4979. [CrossRef] [PubMed]
17. Zhu, C.; Yin, Z.; Lai, W.; Sun, Y.; Liu, L.; Zhang, X.; Chen, Y.; Chou, S.-L. Fe-Ni-Mo Nitride Porous Nanotubes for Full Water Splitting and Zn-Air Batteries. *Adv. Energy Mater.* **2018**, *8*, 1802327. [CrossRef]
18. Yu, Y.; Zhou, J.; Sun, Z. Novel 2D Transition-Metal Carbides: Ultrahigh Performance Electrocatalysts for Overall Water Splitting and Oxygen Reduction. *Adv. Funct. Mater.* **2020**, *30*, 2000570. [CrossRef]
19. Lian, Y.; Sun, H.; Wang, X.; Qi, P.; Mu, Q.; Chen, Y.; Ye, J.; Zhao, X.; Deng, Z.; Peng, Y. Carved Nanoframes of Cobalt–Iron Bimetal Phosphide as a Bifunctional Electrocatalyst for Efficient Overall Water Splitting. *Chem. Sci.* **2019**, *10*, 464–474. [CrossRef] [PubMed]
20. Liu, Y.; Jiang, S.; Li, S.; Zhou, L.; Li, Z.; Li, J.; Shao, M. Interface Engineering of (Ni, Fe)S_2@MoS_2 Heterostructures for Synergetic Electrochemical Water Splitting. *Appl. Catal. B Environ.* **2019**, *247*, 107–114. [CrossRef]
21. Chunduri, A.; Gupta, S.; Bapat, O.; Bhide, A.; Fernandes, R.; Patel, M.K.; Bambole, V.; Miotello, A.; Patel, N. A Unique Amorphous Cobalt-Phosphide-Boride Bifunctional Electrocatalyst for Enhanced Alkaline Water-Splitting. *Appl. Catal. B Environ.* **2019**, *259*, 118051. [CrossRef]
22. Zhang, F.-S.; Wang, J.-W.; Luo, J.; Liu, R.-R.; Zhang, Z.-M.; He, C.-T.; Lu, T.-B. Extraction of Nickel from NiFe-LDH into Ni_2P@NiFe Hydroxide as a Bifunctional Electrocatalyst for Efficient Overall Water Splitting. *Chem. Sci.* **2018**, *9*, 1375–1384. [CrossRef] [PubMed]
23. Xiao, Z.; Wang, Y.; Huang, Y.-C.; Wei, Z.; Dong, C.-L.; Ma, J.; Shen, S.; Li, Y.; Wang, S. Filling the Oxygen Vacancies in Co_3O_4 with Phosphorus: An Ultra-Efficient Electrocatalyst for Overall Water Splitting. *Energy Environ. Sci.* **2017**, *10*, 2563–2569. [CrossRef]
24. Wei, C.; Sun, Y.; Scherer, G.G.; Fisher, A.C.; Sherburne, M.; Ager, J.W.; Xu, Z.J. Surface Composition Dependent Ligand Effect in Tuning the Activity of Nickel–Copper Bimetallic Electrocatalysts toward Hydrogen Evolution in Alkaline. *J. Am. Chem. Soc.* **2020**, *142*, 7765–7775. [CrossRef] [PubMed]
25. Peng, Y.; Lu, B.; Chen, S. Carbon-Supported Single Atom Catalysts for Electrochemical Energy Conversion and Storage. *Adv. Mater.* **2018**, *30*, 1801995. [CrossRef] [PubMed]
26. Feng, C.; Faheem, M.B.; Fu, J.; Xiao, Y.; Li, C.; Li, Y. Fe-Based Electrocatalysts for Oxygen Evolution Reaction: Progress and Perspectives. *ACS Catal.* **2020**, *10*, 4019–4047. [CrossRef]
27. Ortiz Peña, N.; Ihiawakrim, D.; Han, M.; Lassalle-Kaiser, B.; Carenco, S.; Sanchez, C.; Laberty-Robert, C.; Portehault, D.; Ersen, O. Morphological and Structural Evolution of Co_3O_4 Nanoparticles Revealed by in Situ Electrochemical Transmission Electron Microscopy during Electrocatalytic Water Oxidation. *ACS Nano* **2019**, *13*, 11372–11381. [CrossRef] [PubMed]
28. Peng, M.; Shi, D.; Sun, Y.; Cheng, J.; Zhao, B.; Xie, Y.; Zhang, J.; Guo, W.; Jia, Z.; Liang, Z.; et al. 3D Printed Mechanically Robust Graphene/CNT Electrodes for Highly Efficient Overall Water Splitting. *Adv. Mater.* **2020**, *32*, 1908201. [CrossRef] [PubMed]
29. Dinç, S.; Demir, Ü. Electrochemical One-Pot Fabrication of Free-Standing Nanoporous NiCo/ERGO Composite as Bifunctional Electrocatalyst for Enhanced Water Splitting. *Int. J. Hydrogen Energy* **2025**, *158*, 150577. [CrossRef]
30. Yu, C.; Lu, J.; Luo, L.; Xu, F.; Shen, P.K.; Tsiakaras, P.; Yin, S. Bifunctional Catalysts for Overall Water Splitting: CoNi Oxyhydroxide Nanosheets Electrodeposited on Titanium Sheets. *Electrochim. Acta* **2019**, *301*, 449–457. [CrossRef]
31. Guzman-Bucio, D.M.; Gomez-Sosa, G.; Cabrera-German, D.; Torres-Ochoa, J.A.; Bravo-Sanchez, M.; Cortazar-Martinez, O.; Carmona-Carmona, A.J.; Herrera-Gomez, A. Detailed Peak Fitting Analysis of the Ni 2p Photoemission Spectrum for Metallic Nickel and an Initial Oxidation. *J. Electron Spectrosc. Relat. Phenom.* **2023**, *262*, 147284. [CrossRef]
32. Laïk, B.; Richet, M.; Emery, N.; Bach, S.; Perrière, L.; Cotrebil, Y.; Russier, V.; Guillot, I.; Dubot, P. XPS Investigation of Co–Ni Oxidized Compounds Surface Using Peak-On-Satellite Ratio. Application to $Co_{20}Ni_{80}$ Passive Layer Structure and Composition. *ACS Omega* **2024**, *9*, 40707–40722. [CrossRef] [PubMed]
33. Tompkins, B.D.; Fisher, E.R. Evaluation of Polymer Hydrophobic Recovery Behavior Following H_2O Plasma Processing. *J. Appl. Polym. Sci.* **2015**, *132*, 41978. [CrossRef]

34. Xiao, X.; Zhang, X.; Zhang, Z.; You, J.; Liu, S.; Wang, Y. Macro-/Meso-Porous $NiCo_2O_4$ Synthesized by Template-Free Solution Combustion to Enhance the Performance of a Nonenzymatic Amperometric Glucose Sensor. *Microchim. Acta* **2019**, *187*, 64. [CrossRef] [PubMed]
35. Rashid, J.; Gilani, K.; Arif, A.; Saraj, C.S.; Li, W.; Xu, M. Facile Synthesis of NiCo@rGO as Bifunctional Electrocatalyst for Enhanced Water Splitting. *Int. J. Hydrogen Energy* **2024**, *51*, 774–786. [CrossRef]
36. Anantharaj, S.; Noda, S.; Jothi, V.R.; Yi, S.; Driess, M.; Menezes, P.W. Strategies and Perspectives to Catch the Missing Pieces in Energy-Efficient Hydrogen Evolution Reaction in Alkaline Media. *Angew. Chem. Int. Ed.* **2021**, *60*, 18981–19006. [CrossRef] [PubMed]
37. Arunkumar, P.; Gayathri, S.; Han, J.H. A Complementary Co−Ni Phosphide/Bimetallic Alloy-Interspersed N-Doped Graphene Electrocatalyst for Overall Alkaline Water Splitting. *ChemSusChem* **2021**, *14*, 1921–1935. [CrossRef] [PubMed]
38. Dong, J.; Sun, T.; Zhang, Y.; Zhang, H.; Lu, S.; Hu, D.; Chen, J.; Xu, L. Mesoporous NiCo Alloy/Reduced Limani Nanocomposites as Efficient Hydrogen Evolution Catalysts. *J. Colloid Interface Sci.* **2021**, *599*, 603–610. [CrossRef] [PubMed]
39. Zhang, W.; Zhang, B.; Li, Y.; Zhang, E.; Zhang, Y.; Wang, Q.; Cong, Y. Multi-Active Site CoNi-MOFs as Non-Noble Bifunctional Electrocatalysts for Highly Efficient Overall Water Splitting. *Int. J. Hydrogen Energy* **2022**, *47*, 1633–1643. [CrossRef]
40. Marcano, D.C.; Kosynkin, D.V.; Berlin, J.M.; Sinitskii, A.; Sun, Z.; Slesarev, A.S.; Alemany, L.B.; Lu, W.; Tour, J.M. Correction to Improved Synthesis of Graphene Oxide. *ACS Nano* **2018**, *12*, 2078. [CrossRef] [PubMed]
41. Tien, H.N.; Luan, V.H.; Hoa, L.T.; Khoa, N.T.; Hahn, S.H.; Chung, J.S.; Shin, E.W.; Hur, S.H. One-Pot Synthesis of a Reduced Graphene Oxide–Zinc Oxide Sphere Composite and Its Use as a Visible Light Photocatalyst. *Chem. Eng. J.* **2013**, *229*, 126–133. [CrossRef]
42. Li, L.; Limani, N.; Pantony, R.; Dieckhöfer, S.; Santana Santos, C.; Schuhmann, W. Au Micro- and Nanoelectrodes as Local Voltammetric pH Sensors During Oxygen Evolution at Electrocatalyst-Modified Electrodes. *Small Sci.* **2024**, *4*, 2300283. [CrossRef] [PubMed]
43. Goswami, A. *Thin Film Fundamentals*; New Age International: New Delhi, India, 1996; ISBN 978-81-224-0858-4.

Disclaimer/Publisher's Note: The statements, opinions and data contained in all publications are solely those of the individual author(s) and contributor(s) and not of MDPI and/or the editor(s). MDPI and/or the editor(s) disclaim responsibility for any injury to people or property resulting from any ideas, methods, instructions or products referred to in the content.